KRISTIN KWAKWA 8/31/2021 JOURNAL CLUB

SCIENCE ADVANCES | RESEARCH ARTICLE

CANCER

Breast cancer–secreted factors perturb murine bone growth in regions prone to metastasis

Aaron E. Chiou[1]*†, Chuang Liu[2]*‡, Inés Moreno-Jiménez[2], Tengteng Tang[2], Wolfgang Wagermaier[2], Mason N. Dean[2§], Claudia Fischbach[1,3‖], Peter Fratzl[2‖]

Breast cancer frequently metastasizes to bone, causing osteolytic lesions. However, how factors secreted by primary tumors affect the bone microenvironment before the osteolytic phase of metastatic tumor growth remains unclear. Understanding these changes is critical as they may regulate metastatic dissemination and progression. To mimic premetastatic bone adaptation, immunocompromised mice were injected with MDA-MB-231–conditioned medium [tumor-conditioned media (TCM)]. Subsequently, the bones of these mice were subjected to multiscale, correlative analysis including RNA sequencing, histology, micro–computed tomography, x-ray scattering analysis, and Raman imaging. In contrast to overt metastasis causing osteolysis, TCM treatment induced new bone formation that was characterized by increased mineral apposition rate relative to control bones, altered bone quality with less matrix and more carbonate substitution, and the deposition of disoriented mineral near the growth plate. Our study suggests that breast cancer–secreted factors may promote perturbed bone growth before metastasis, which could affect initial seeding of tumor cells.

INTRODUCTION

Bone metastasis is a leading cause of morbidity and mortality in patients with advanced breast cancer (*1*, *2*). Nevertheless, therapeutic strategies to prevent bone metastasis are lacking, due, in part, to limited understanding of the mechanisms that enable breast cancer cells to seed and eventually develop secondary tumors in the skeleton. Disseminated tumor cells (DTCs) that have spread from the primary breast tumor to bone can colonize early in tumorigenesis (*3*). This process is potentially facilitated by circulating factors from the primary tumor preparing the bone microenvironment well in advance of metastasis (*4*, *5*). Most research to date has focused on identifying the molecular and cellular signals regulating DTC fate in bone marrow (*6*–*9*) and areas of active bone deposition (*10*–*12*). However, less is known about whether the structural or chemical properties of the existing bone tissue play roles in supporting DTC seeding, survival, and growth. Further, it remains largely unclear whether premetastatic modifications to the bone matrix occur that contribute to the regulation of DTC fate.

Bone tissue is a naturally dynamic material, and its characteristics may influence key processes of both bone metastasis latency and progression (*5*, *13*–*17*). More specifically, bone matrix is a hierarchically structured composite, consisting primarily of collagen fibrils embedded with aligned nanosized carbonated hydroxyapatite (HA) mineral crystals (2 to 7 nm thick) (*18*) and is regularly locally remodeled through a sequential process of matrix degradation by osteoclasts followed by new deposition by osteoblasts. These bone-resident cell types are known respectively to drive tumor-associated osteolysis (*19*) and DTC colonization (*11*). Yet, whether the bone matrix that they are responsible for maintaining plays any role in regulating metastasis progression remains oddly underappreciated. For example, it is conceivable that aspects of the mineral itself play a role, as HA can critically influence bone biomechanical properties (*18*), cell adhesion, and growth (*15*, *16*) and can vary as a function of anatomical site, age, and disease (*20*–*22*). However, to fully understand the materials properties that contribute to the bone metastatic niche, both the organic and inorganic components of bone must be examined specifically within regions to which DTCs localize, which requires a spatial resolution that exceeds the capacity of standard molecular biology approaches. Application of high-resolution physical sciences techniques to cancer research has great potential to reveal physicochemical changes to bone matrix that have translational relevance. For example, using x-ray scattering techniques and Raman imaging, we recently identified that the proximal tibia of mice, a region frequently targeted by bone metastasis, contains less mature (less crystalline) HA crystals relative to regions not targeted by metastasis and that HA immaturity is further enhanced in mice carrying primary (mammary) tumors (*14*). Because HA crystal size, crystallinity, and carbonate substitution can affect breast cancer cell adhesion and growth (*14*–*17*), understanding whether bone mineral is affected by primary tumor–derived circulating factors, in which bone regions, and at which level of its architecture, may help uncover previously unidentified mechanisms that regulate the initiation of bone metastasis.

To examine the effects of tumor-derived factors in a premetastatic mouse model, we combined histology, confocal laser scanning microscopy, and RNA sequencing (RNA-seq) analysis of bones with multiscale, correlative bone materials characterization techniques including micro–computed tomography (micro-CT), dynamic histomorphometry, Raman imaging, and small-angle x-ray scattering (SAXS) (Fig. 1A). We focused our analysis on trabecular bone in proximity to the growth plate as well as endocortical bone, given that DTCs seed both regions in mouse models of early-stage bone metastasis (*11*, *12*, *23*). We demonstrate that circulating tumor–secreted factors regulate bone matrix properties even before metastatic

---

[1] Nancy E. and Peter C. Meinig School of Biomedical Engineering, Cornell University, Ithaca, NY 14853, USA. [2] Department of Biomaterials, Max Planck Institute of Colloids and Interfaces, 14424 Potsdam, Germany. [3] Kavli Institute at Cornell for Nanoscale Science, Cornell University, Ithaca, NY 14853, USA.
*These authors contributed equally to this work.
†Present address: Department of Biomedical Data Science, Stanford University, Stanford, CA 94305, USA.
‡Present address: College of Oceanography, Hohai University, Nanjing, Jiangsu 210098, China.
§Present address: Department of Zoology, School of Natural Sciences, Trinity College Dublin, Dublin 2, Ireland.
‖Corresponding author. Email: fratzl@mpikg.mpg.de (P.F.); cf99@cornell.edu (C.F.)

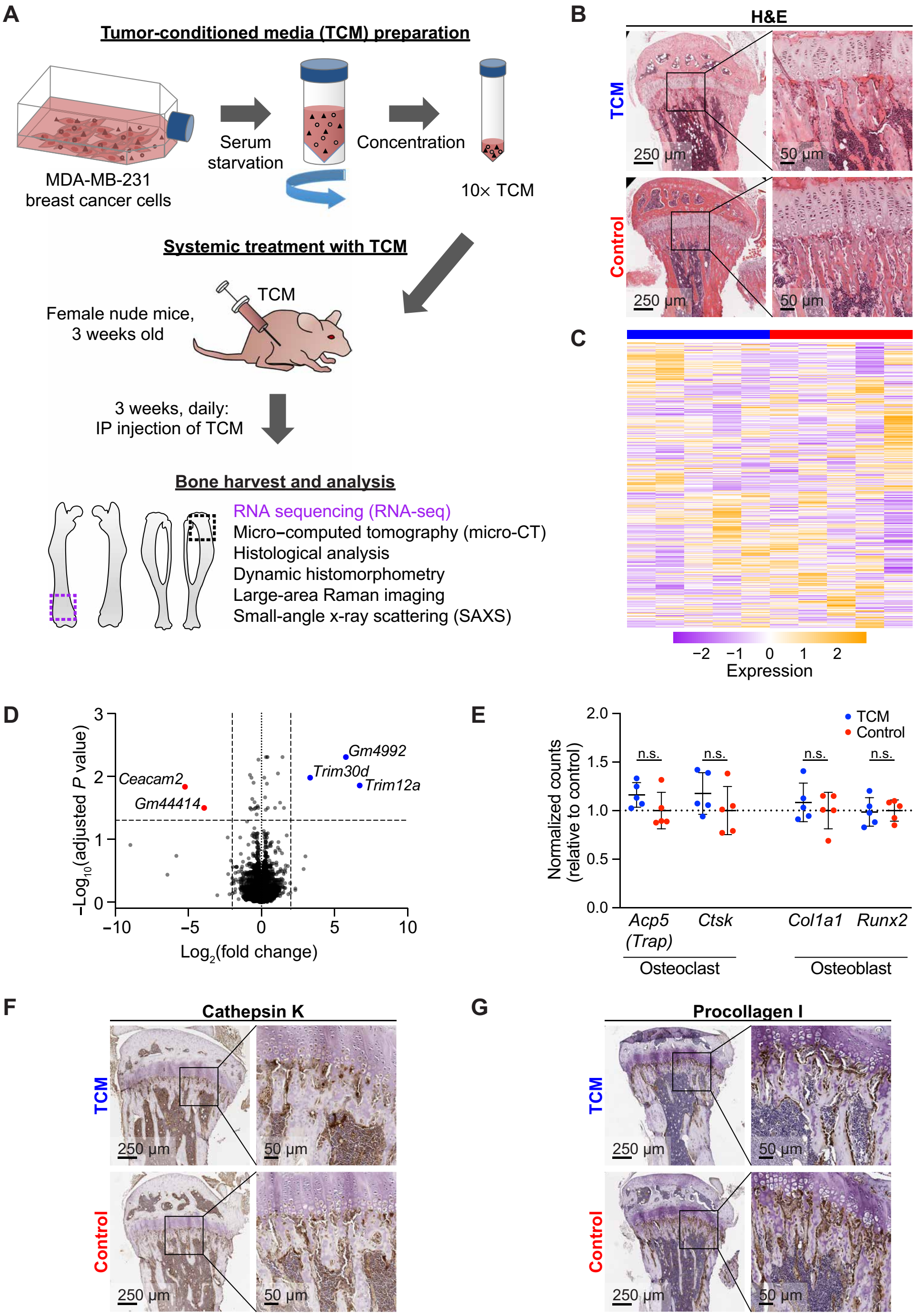

Fig. 1. Experimental setup, histological analysis, and RNA-seq of murine hindlimbs. (**A**) Schematic of experimental design. TCM was prepared from cultures of MDA-MB-231 breast cancer cells and then injected into 3-week-old female nude mice daily, for a period of 3 weeks. Bones (both tibiae and femora) were harvested and analyzed using complementary biological and physical sciences approaches. IP, intraperitoneal. Representative (**B**) hematoxylin & eosin (H&E)–stained histological cross sections of decalcified tibiae. (**C**) Heatmap of all genes analyzed via RNA-seq analysis of marrow-removed trabecular bone from femora (rows hierarchically clustered; see the Supplementary Materials for full size heatmap with dendrograms). Heatmap color/intensity represents the expression levels, as calculated by centering and scaling normalized count values in the row direction (per gene). (**D**) Volcano plot indicates which genes were significantly differentially expressed. Of 18,843 unique genes sequenced, 5 genes were differentially expressed (0.027% of total) with the criteria of adjusted $P < 0.05$ and $\log_2$ fold change >2. (**E**) Normalized counts for selected osteoclast- and osteoblast-specific genes (see the Supplementary Materials for additional bone-relevant genes). (n.s., adjusted $P > 0.05$). Representative (**F**) cathepsin K– and (**G**) procollagen I–stained histological cross sections of decalcified tibiae.

dissemination, suggesting that tumors are distantly preparing skeletal metastatic sites via an "advance team" of secreted factors. Materials perspectives on how cancers construct suitable environments are vital for anticipating and obviating metastasis. Results from this work therefore have potential functional consequences for the pathogenesis and treatment of bone metastasis while also revealing prognostic/diagnostic materials signatures that can presage DTC seeding in bones.

RESULTS

Circulating tumor–secreted factors do not affect mouse growth or bone cell activity

To model the effects of circulating tumor–secreted factors on the bone microenvironment in vivo, we intraperitoneally injected tumor-conditioned media (TCM) collected from MDA-MB-231 breast cancer cells into female nude mice daily for a period of 3 weeks (Fig. 1A). The concentration of injected factors was consistent with that mediated by a primary tumor. First, we confirmed that this treatment did not affect the growth of these mice, as weight gain over the course of the experiment did not differ between TCM and control mice (fig. S1A). Similarly, we verified from micro-CT data that tibia length was similar between experimental and control groups (fig. S1B) while also verifying from histology and backscattered electron imaging that growth plate morphology and thickness in the proximal tibiae [i.e., a frequent site of metastasis in these mice (*24*, *25*)] were similar between experimental and control groups (Fig. 1B and fig. S1, C and D).

Bone cell activity is vital to the structuring of bone matrix and therefore has potential to inform our understanding of premetastatic bone alterations. To broadly assess whether TCM treatment led to transcriptional changes in the bones, we performed RNA-seq analysis of distal femora isolated from the same mice as the tibiae used for histology. Given our focus on bone matrix, we isolated RNA from bone tissue following removal of the marrow as described previously (fig. S2A) (*26*). To our surprise, gene expression did not vary substantially between control and TCM-treated mice, as suggested by a lack of clustering within conditions via heatmap visualization and principal components analysis (Fig. 1C, and figs. S2, B and C, and S3). Only five genes were differentially expressed between experimental groups (0.027% of total sequenced) (Fig. 1D), none of which have clear biological association with bone remodeling processes. Accordingly, differential gene expression analysis of osteoclast- and osteoblast-specific genes indicated that TCM treatment did not affect osteoclast or osteoblast activation in our model (Fig. 1E and fig. S2D). These findings were further supported by immunohistochemistry (IHC) analysis of cathepsin K (a matrix-degrading proteinase expressed by osteoclasts) and procollagen I (a collagen I precursor expressed by matrix-producing osteoblasts), which indicated that the activity of these cell types did not differ between tibiae of TCM-treated and control mice (Fig. 1, F and G, and fig. S4).

While RNA-seq analysis and histology are routinely used to examine the role of the microenvironment in bone metastasis, alterations in bone matrix properties are equally important but may not be detectable at the transcriptional level. To explore whether the bones of TCM-treated mice exhibit distinct physicochemical properties, we next analyzed our samples with a toolbox of multiscale bone materials characterization techniques.

TCM stimulates abnormal bone growth in trabecular and cortical bone in mice proximal tibia

Overall differences in bone cell activity were not apparent between the bones of control and TCM-treated mice transcriptionally or histologically; however, to determine whether TCM treatment caused global microstructural changes to bone matrix and tissue architecture, we digitally separated trabecular and cortical regions of micro-CT–scanned tibiae and performed quantitative morphometric analyses, comparing the volumes and arrangements of bone tissue.

Our analysis demonstrated distinct structural differences in the arrangement and morphology of trabecular bone between control and TCM-injected animals (Fig. 2A), despite there being no difference in the total volume of the endocortical space occupied by trabecular bone or volume of the trabecular bone itself (although the latter tended to be larger in TCM mice) (Fig. 2B). Compared with the tibiae of control mice, those from TCM-treated mice had fewer trabeculae (12.4% lower trabecular number) but more trabecular bone tissue per unit volume (11.3% higher bone volume fraction), more variable trabecular thickness (fig. S5A) with thicker trabeculae on average (21.2% greater trabecular thickness), and more widely spaced trabeculae (18.9% greater trabecular separation) (Fig. 2B). As a result of TCM mice having fewer, thicker, and more sparsely distributed trabeculae, the bone surface/bone volume ratio of the TCM group was decreased by 10.6% compared to the control group (fig. S5B). All other structural parameters describing trabecular bone morphology were similar between the two groups, including degree of anisotropy (a measure of preferred orientation and coalignment of trabeculae), structural model index (a method for determining whether trabeculae are more rod- or plate-like in their cross-sectional geometry, the latter of which tends to be more load bearing), and connectivity (the total number of connections in a trabecular bone network) (fig. S5, C to E). These results suggest that TCM treatment resulted in an increase in the bone volume fraction of trabecular bone in our model by increasing trabecular thickness, despite an overall reduction in the number of trabeculae and an increase in the distance between them (Fig. 2C).

Micro-CT also revealed a marked difference in the structure of cortical bone between control and TCM-injected animals (Fig. 2D). TCM treatment did not affect the overall size of the bone (i.e., the total volume of bone and endocortical space enclosed within the periosteum) but resulted in an increase in cortical bone volume and, therefore, in the bone volume fraction (10.1 and 11.6% higher, respectively) (Fig. 2E). As a result, the bone surface/bone volume ratio of the TCM group was decreased by 10.6% compared to the control group (Fig. 2E). Compared to that of the control group, the cortical bone of TCM-treated mice was thicker (by 20 μm on average, Fig. 2F), suggestive of endocortical thickening. Further, TCM-treated mice exhibited increased cross-sectional area (10 to 26% larger; Fig. 2G) with a corresponding 30 to 40% increase in polar moment of inertia (fig. S5F) in their cortical bone compared to the control group. However, these geometric changes alone should be interpreted alongside alterations in bone materials properties to predict impact on bone mechanical function. For example, while an increased cross-sectional area could increase resistance to bending and torsion, it could instead reflect altered bone quality and subsequent compensatory growth (*27*); therefore, to gain insight into this potential mechanical adaptation, we next sought to characterize dynamics, composition, and organization of the bone tissue.

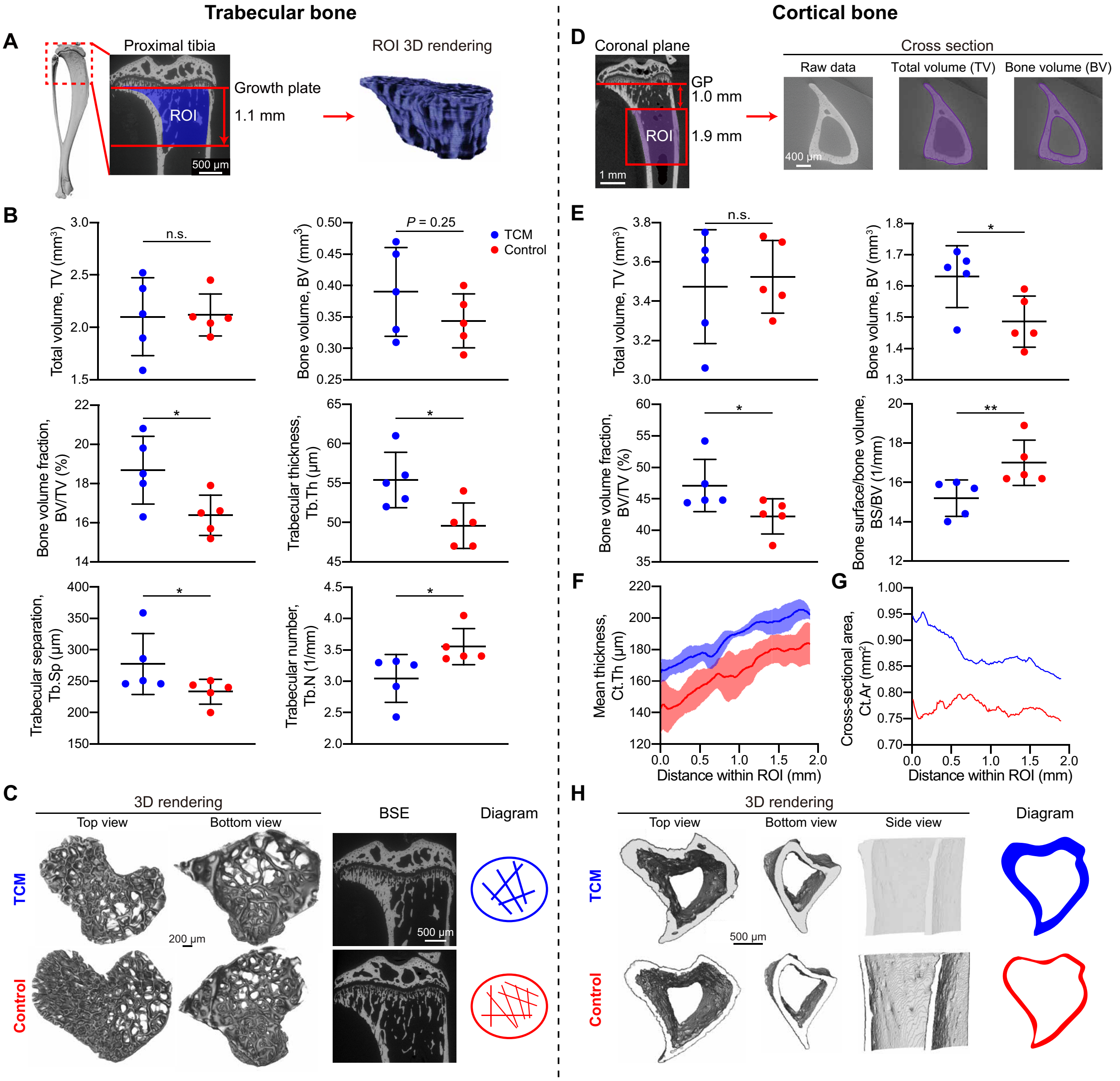

Fig. 2. TCM stimulates abnormal bone growth in the proximal tibia. (**A**) A micro-CT 3D surface rendering of a mouse tibia and a backscatter scanning electron (BSE) image of the proximal tibia showing the analyzed region of interest (ROI), which is 1.1 mm in height beneath the growth plate to capture most of the trabecular bone. The ROI 3D rendering shows the total volume that includes the trabecular bone (blue) and trabecular space (black). (**B**) Quantification of total volume (TV), trabecular bone volume (BV), bone volume fraction, trabecular thickness, trabecular separation, and trabecular number. (**C**) Micro-CT 3D surface-rendering images of the trabecular bone viewed from the top (first) and bottom (second), BSE images (third), and diagrams representing the trabecular bone microstructural comparison (fourth). (**D**) Micro-CT image showing the ROI in the proximal tibia of mice, which is 1.9 mm in height beneath the growth plate (GP) with an offset of 1.0 mm to capture mature cortical bone. The total volume is the volume inside periosteum; total volume equals the sum of bone volume and volume inside endosteum. (**E**) Quantification of total volume, bone volume, bone volume fraction, and bone surface/bone volume ratio. (**F**) The cortical thickness and (**G**) the cross-sectional area of cortical bone as a function of distance within the ROI are plotted. In (F), mean values and the SD of five samples are shown, while in (G), mean values are shown. (**H**) 3D rendering images of cortical bone from the TCM and control mice and diagrams describing the geometric change. (n.s., $P > 0.05$; *$P < 0.05$; **$P < 0.01$; $n = 5$, unpaired t test).

TCM treatment increases mineral apposition in the endocortical bone of murine proximal tibiae

On the basis of the increased thickness of both trabecular and cortical bone in TCM-treated mice, we next examined whether those microstructural changes were correlated with global alterations to mineral density and collagen structure, two key parameters determining the materials properties of bone. However, we found that TCM changed neither mineral density nor collagen structure, as evidenced by backscatter scanning electron microscopy (BSE; fig. S6A) and second harmonic generation imaging (fig. S6B), respectively. This indicated that the bone matrix at a general, tissue-level length scale was similarly organized between conditions. However, these analyses did not clarify whether TCM treatment could locally affect bone materials properties in regions of the tibia that are subject to higher rates of bone formation (and differential deposition between the two treatments).

To shed light on the spatiotemporal dynamics of new bone formation and existing matrix turnover as a function of TCM treatment, we determined the rate and nature of new mineral apposition using dynamic histomorphometry. For these experiments, mice were sequentially injected with different mineral-binding dyes 1 week apart (calcein at 13 days and then xylenol orange at 20 days after the start of the experiment) (Fig. 3A), a procedure by which the bone deposited in the 7-day gap between the two injections is indicated according to its location between the dye bands. Although double-labeling (both calcein and xylenol orange) was found in most cortical bone, some trabecular bone, and epiphyseal bone (Fig. 3B), it was absent in growth plate–adjacent bone, where only xylenol orange labeling

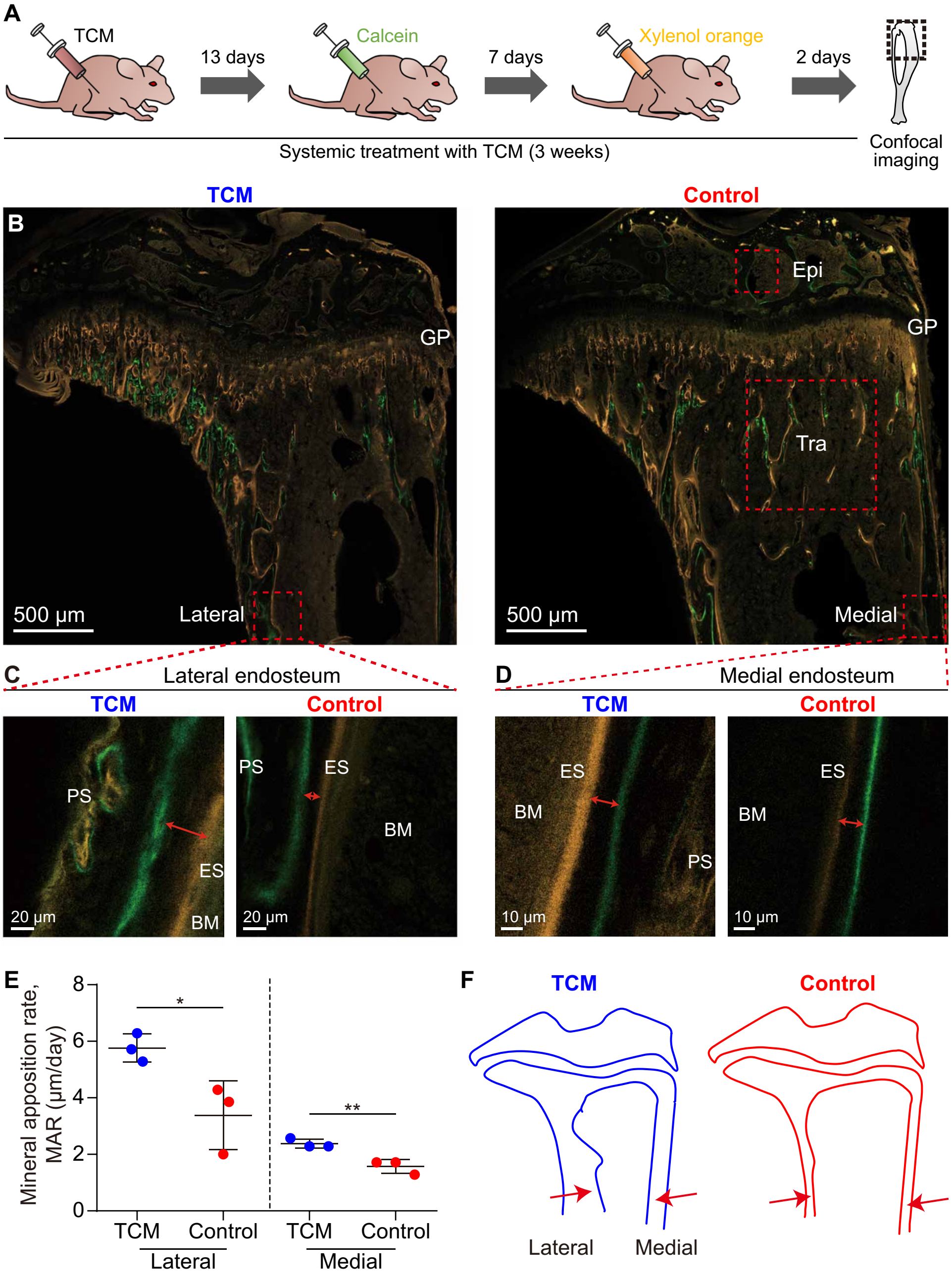

Fig. 3. TCM increases mineral apposition rate in the endocortical bone. (**A**) Schematic showing the injection of calcein and xylenol orange into mice 7 days apart before the sacrifice of mice. (**B**) Overlay confocal laser scanning microscopy images of representative proximal tibiae of the TCM and control mice in which green is calcein while orange is xylenol orange. In both groups, epiphyseal bone (Epi), trabecular bone (Tra; see the Supplementary Materials), lateral cortical bone, and medial cortical bone are analyzed (red dashed boxes). Magnified images of the calcein and xylenol orange labeling in the (**C**) lateral and (**D**) medial cortical bone periosteum. Red arrows indicate the distance between the two labels. PS, periosteum; ES, endosteum; BM, bone marrow. (**E**) Quantification of the MAR (the distance between the midpoints of two consecutive labels divided by the time between the midpoints of the labeling periods, 7 days) of the two groups. (**F**) Diagrams showing increased bone formation in the endosteum of the cortical bone in the TCM group. (*$P < 0.05$; **$P < 0.01$; $n = 3$, unpaired *t* test).

was observed. This indicates that this region experienced high rates of turnover (i.e., the removal of calcein-labeled tissue) and/or delayed new bone deposition (i.e., after the day-13 calcein injections) (Fig. 3B).

The calcein and xylenol orange labels created temporal reference lines in the bone matrix, allowing us to quantitatively explore TCM-mediated differences in the physiological process of bone mineralization. To hone in on the local deposition differences that contributed to the structural variations that we observed with micro-CT, we measured the distance between consecutive labels and divided by the time between injections to calculate the mineral apposition rate (MAR) for epiphyseal, trabecular, and cortical bone (both lateral and medial sides) (Fig. 3, C and D). Notably, the MAR of the endocortical bone was higher in the TCM relative to the control group (~1.7× and ~ 1.5× greater in lateral and medial sites, respectively) (Fig. 3E). In contrast, periosteal cortical bone showed a high degree of variability in staining, with many investigated regions of interest (ROIs) not double-labeled or exhibiting very narrow bands of growth that were within the error of our measurement technique and therefore were not quantified. Qualitatively, however, the MAR of periosteal cortical bone did not differ between groups and was overall much smaller (fig. S7A). The MAR of epiphyseal and trabecular bone was similar between groups (fig. S7, B and C). These findings support the endocortical thickening that we observed via micro-CT by demonstrating that TCM yields a location-specific difference in new mineral apposition, with a focal increase in the deposition of endocortical bone, an important bone metastasis niche (*12*, *28*), but no obvious concomitant change to periosteal cortical bone deposition (Fig. 3F).

TCM alters the quality of cortical and trabecular bone in the proximal tibia of mice

To examine whether the observed TCM-mediated changes in endocortical bone MAR and trabecular bone structure were accompanied by changes in bone matrix quality (i.e., material-level characteristics of bone mineral and collagen), we used Raman spectroscopy to compare mineral-to-matrix and B-type carbonate-to-mineral ratios in tibiae. For the mineral-to-matrix ratio, we used Raman bands that are nearly independent of the laser polarization direction (*29*). While a higher mineral-to-matrix ratio reflects increased tissue maturity, greater B-type carbonate substitution (for phosphate in the apatite lattice) is known to increase with age in mice (*30*). In addition, we examined orientation effects in tissue architecture by performing Raman imaging with two different polarization angles of the exciting laser (0° and 90°), because certain Raman signal intensities depend strongly on the collagen fiber orientation (e.g., ν_1 PO_4, which is strongly polarization-dependent in contrast to ν_2 PO_4) (*29*). To determine the potential for local differences in bone quality in regions of new bone deposition, we conducted this analysis on double-labeled trabecular and medial endocortical bone (i.e., tissue deposited, but not remodeled, during the study period), as the latter region exhibited pronounced MAR changes between TCM and control mice. In the medial endosteum, both the mineral-to-matrix ratio and the carbonate-to-mineral ratio were increased (by 23 to 45% and 15 to 25%, respectively) in the TCM versus the control group, regardless of laser polarization angle (Fig. 4, A to E, and fig. S8, A and B). Similar changes were also detected in trabecular bone (Fig. 4F and fig. S8, C to E), despite no obvious differences between groups in trabecular bone MAR (fig. S7C). This indicates that TCM treatment led to increased mineral density and apatite with higher carbonate for phosphate substitution in regions of new bone deposition.

To characterize how TCM may affect the organic bone matrix, we also determined the ratio of Raman signal intensities between the spectral regions associated with the CH_2-wag vibration and amide III (fig. S8F). Both spectral regions are characteristic of the organic matrix (*31*), and this ratio has previously been used to estimate the amount of total organic molecule content relative to matrix proteins (*32*). Modified values of the CH_2-wag band have also been observed in some types of malignant tissues (*33*). In control mice, we found that this parameter was high in newly formed bone but gradually decreased with tissue maturity, leveling off in older tissue (fig. S8, G and H). Whereas mature bone exhibited similar values between groups, this parameter was decreased in newly formed bone of TCM-treated relative to control mice, remaining at a value similar to mature bone (fig. S8, G and H). Overall, Raman analysis of the bone matrix suggests that TCM accelerated the maturation of newly formed bone, increasing its mineral-to-matrix ratio and reducing its CH_2-wag/amide III ratio more quickly (Fig. 4A and fig. S8A).

As BSE images of the endocortical and trabecular bone (fig. S6, C and D) revealed no obvious mineral density differences between groups, we performed IHC to determine whether the detected changes in mineral quality were accompanied by specific alterations in organic matrix composition. We focused on osteopontin, a key extracellular matrix component involved in bone mineralization (*34*) that is less abundant in older bone tissue (*35*). Image analysis of immunostained histological cross sections suggested that TCM treatment decreased osteopontin levels (Fig. 4G). Collectively, these data suggest that TCM treatment affects the mineral quality in both newly deposited endocortical and trabecular bone by increasing both the mineral-to-matrix and carbonate-to-mineral ratios toward characteristically more mature mineral (*22*, *36*). These changes were accompanied by more mature organic matrix and decreased levels of osteopontin, an organic bone matrix component that can inhibit mineralization (*18*, *34*, *37*), which could explain the increased mineral-to-matrix ratio.

TCM does not affect mineral nanostructure in regions with altered bone quality

Our Raman analyses indicated that TCM mediates crystallographic differences in newly formed cortical and trabecular bone, but it was not clear whether these differences were correlated with changes in mineral nanostructure (e.g., mineral thickness, orientation, and arrangement), a feature that may influence tumor cell behavior (*15*). We quantified mineral crystal shape and spacing parameters in different anatomical regions of the tibiae (epiphysis, mineralized cartilage, trabeculae, and cortex) at ~100-μm resolution using scanning SAXS (fig. S9A). Despite the intergroup differences observed at larger length scales, interestingly, TCM treatment appeared to have no effect on mineral crystal thickness or degree of orientation (as expressed by the T and ρ parameters, respectively) regardless of anatomical location (fig. S9, B and C). Similarly, mineral arrangement [the intermineral particle distance and its regularity, as described by the $G(x)$ function derived from SAXS patterns] showed no difference between groups in all four regions analyzed (fig. S10A). Even when focusing specifically on the endocortex, the region that exhibited the most pronounced differences in MAR and bone quality between TCM and control mice (Figs. 3F and 4, A to D), both groups exhibited similar mineral parameters [$G(x)$ function shape,

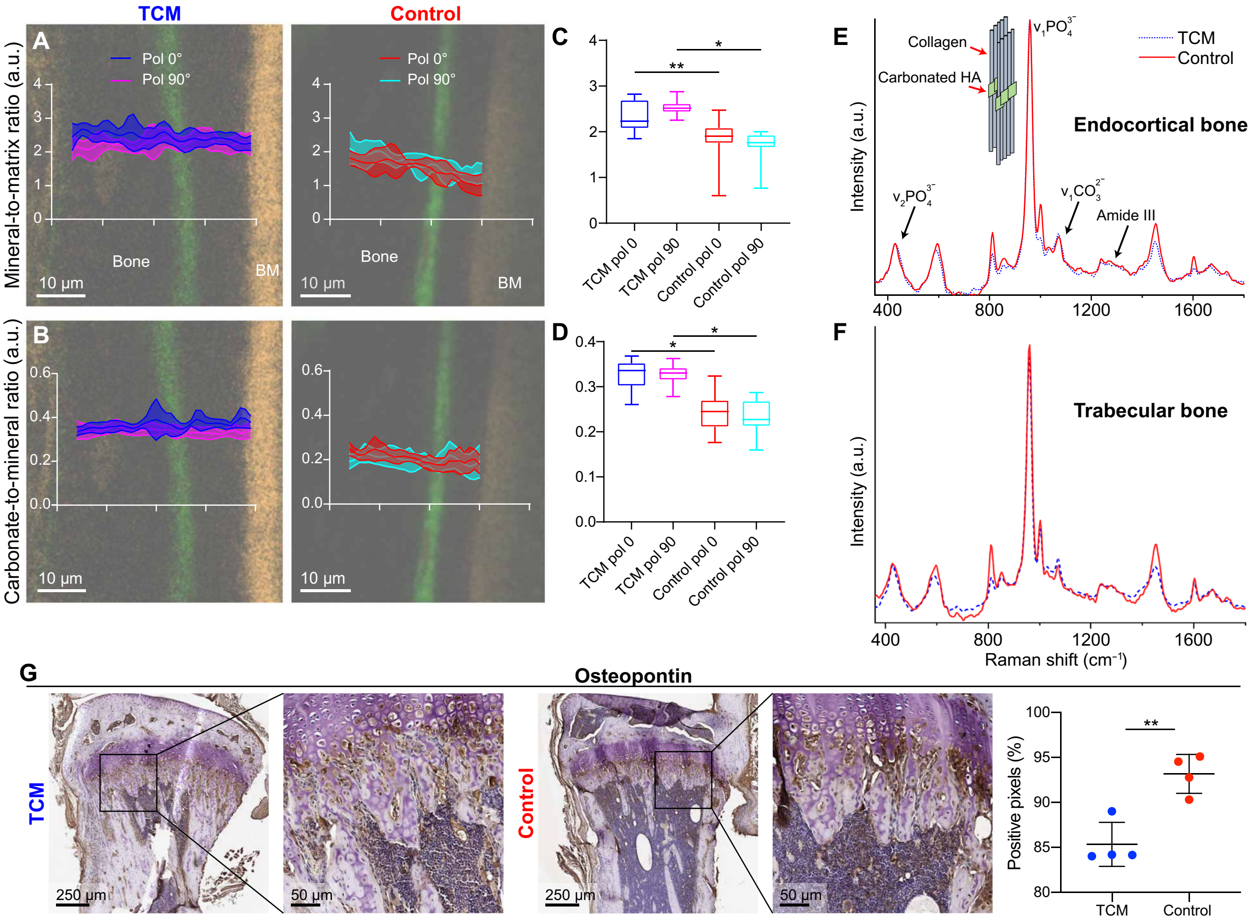

Fig. 4. TCM alters bone quality in the endocortical and trabecular bone. (**A**) Mineral-to-matrix ratio ($v_2\ PO_4^{3-}$ /amide III) and (**B**) carbonate-to-mineral ratio ($v_1\ CO_3^{2-}/v_2\ PO_4^{3-}$) of the TCM and control group under 0° and 90° polarizations (pol) of the incident laser beam using Raman analysis. The ratio graphs are superimposed on the bone dynamic histomorphometry images in which the space between calcein (green) and xylenol orange (orange) labels is newly formed bone. Medial endosteal bone was examined as this region had more pronounced and robust MAR changes among samples. Mean values and SD are shown in the plots. a.u., arbitrary units. Box-and-whisker plots show the (**C**) mineral-to-matrix and (**D**) carbonate-to-mineral ratio statistics in the newly formed bone between the two labeling lines. The boxes represent 50% of the data, limited by the upper and lower quartiles, with the median indicated by a line within each box. The vertical lines indicate the range of the data; $N = 3$ in each group (TCM pol 0° and 90° and control pol 0° and 90°), and 600 (~200 from each animal) Raman spots are collected in each group. $^*P < 0.05$, $^{**}P < 0.01$, one-way analysis of variance (ANOVA) with Tukey's multiple comparisons test. Representative Raman spectra of the newly formed (**E**) medial endocortical bone and (**F**) trabecular bone from the two groups. (**G**) IHC staining of osteopontin was conducted, and percentage of positive pixels within 200 μm of the growth plate was quantified using Aperio ImageScope. Graphs represent means ± SD of values. ($^{**}P < 0.01$; $n = 3$ to 5 samples per condition; Welch's unequal variances t test).

T parameter, and ρ parameter; fig. S10, B to E). The only significant difference was a decrease in the orientation of the mineral particles very close to the growth plate in TCM-treated mice (Fig. 5), a region where tumor-mediated nanostructural changes of mineral (*14*) and initial seeding of bone metastasis (*24*, *25*) have been detected. Improved spatial resolution afforded by synchrotron-based SAXS may be necessary to further investigate the mineral nanostructure in this region. Together, our earlier analyses indicated that TCM-mediated microscale differences in bone structure and quality occurred at multiple anatomical locations, but nanoscale differences in mineral particle thickness, orientation, and arrangement were largely undetectable using conventional SAXS analysis.

DISCUSSION

Our study has demonstrated that although breast cancer metastasis eventually causes bone loss, tumor-derived factors can cause local alterations to both bone architecture and quality without direct contact between tumor and bone cells. Tumor-derived factors stimulated site-specific, abnormal bone growth premetastatically in both the trabecular and endocortical bone of the proximal tibia. In addition, the quality of the newly formed bone was altered relative to control conditions as suggested by higher mineral-to-matrix and carbonate-to-mineral ratios, decreased deposition of organic bone matrix, and less oriented mineral crystals in trabecular bone near the growth plate. These changes appear to occur at a particular and largely unexamined scale of the bone tissue: neither at the level of overall bone cell composition nor in the construction of the mineral itself but in where and how the cells assemble the matrix that tumor cells subsequently target for metastasis.

Given the prevalence of osteolysis in clinically detectable metastatic disease, current efforts to alleviate bone metastasis–associated symptoms center on targeting the behavior of osteoclasts, with agents such as bisphosphonates and the receptor activator of nuclear

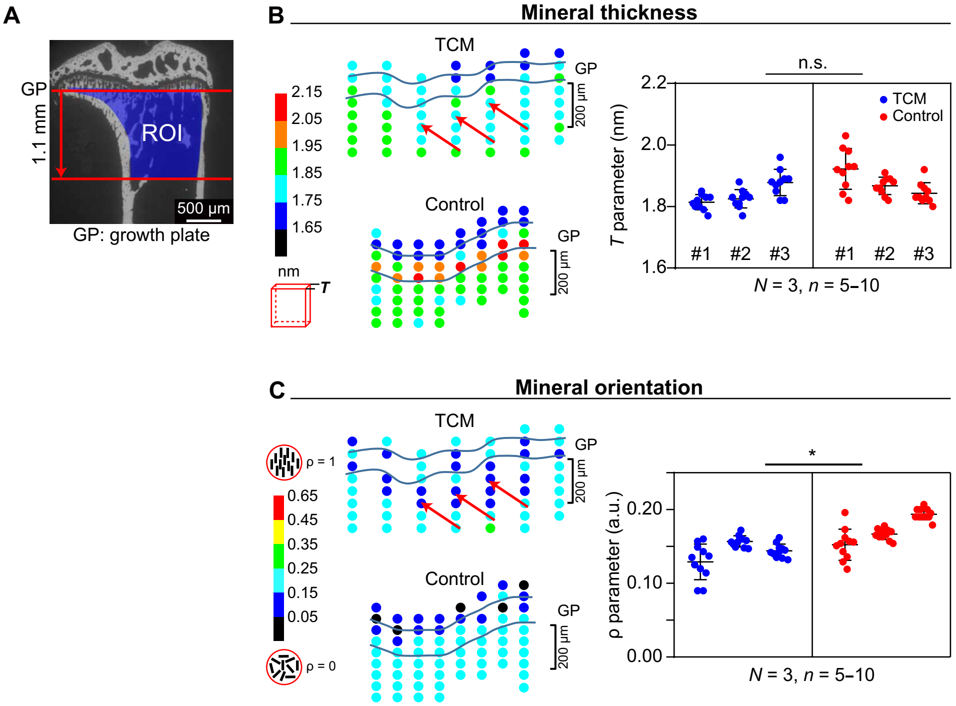

Fig. 5. TCM alters bone structure most near the growth plate region. (**A**) A BSE image of the proximal tibia highlighting the trabecular bone beneath the GP that was analyzed using SAXS. (**B**) Color-coded *T* parameter (mineral thickness) and quantification (from SAXS analysis) of three murine tibiae. Red arrows indicate the bone regions that have smaller *T* parameter in the TCM group compared to that of the control group. (**C**) Color-coded ρ parameter (mineral orientation) and quantification (from SAXS analysis) of three mouse tibiae. Red arrows indicate the bone regions that have smaller ρ parameter in the TCM group compared to that of the control group. Graphs represent mean ± SD (n.s., $P > 0.05$; *$P < 0.05$; $N = 3$ mice, $n = 5$ to 10 spots per mouse tibia; nested *t* test).

factor-κB ligand–neutralizing antibody denosumab approved for clinical use (*38*). Recent clinical trials have also focused on the use of bisphosphonates as an adjuvant therapy to prevent bone metastasis, motivated by findings that bone metastatic tumor growth is driven by dysregulated bone remodeling where osteolysis is favored (*39*). Unfortunately, these treatments do not consistently reduce metastatic tumor burden or improve patient survival (*40*), highlighting the need for new strategies to prevent or reduce bone metastasis (*41*). In contrast to focusing on late-stage osteolytic disease, the development of improved treatments for bone metastasis may benefit from deeper understanding of the mechanisms underlying early-stage colonization and survival in the bone microenvironment, which elude clinical detection. Our data combined with previous findings that DTCs depend on direct contact with bone-forming cells to colonize and proliferate within bone (*11*) and that tumor cells secrete factors that expand osteoblast populations (*42*) suggest that therapeutic targeting of osteogenic cells may present a promising alternative strategy. While osteolysis is predominant in late-stage metastasis, early stages may depend on a different microenvironmental context (i.e., deposition of new bone matrix) to support DTC adhesion and transition into micrometastasis. Our study highlights that bone formation is altered in the presence of tumor-secreted factors, supports prior evidence that tumor-mediated bone adaptation varies considerably between early and late stages of bone metastasis, and underscores the importance of understanding the impact of these changes on bone physiology and metastasis to inform therapeutic targeting.

While the increase in both cortical and trabecular bone thickness that we have observed in TCM-injected mice could result from tumor-derived signals directly promoting bone-forming cell behavior to prepare a bone metastatic niche, it may also be reflective of mechanical adaptation compensating for bone quality changes. Accumulating evidence suggests that tumors induce the formation of premetastatic niches or microenvironments in distant organs that are favorable for the survival and outgrowth of tumor cells (*43*). Extracellular vesicles released by breast cancer cells, for example, can target the bone microenvironment, where they are primarily taken up by osteoclasts, osteoblasts, and some bone marrow cells (*44*). While TCM injections do not model sustained release of primary tumor–derived factors, the TCM injections in this study systemically delivered both soluble factors and extracellular vesicles at concentrations similar to xenograft models (*45*). Whereas TCM caused no change to periosteal cortical bone, it stimulated more and faster matrix formation in the endocortical bone, an osteoblast-rich niche that has been shown to support homing of prostate cancer cells to bone (*12*, *28*). The observed endocortical thickening absent of periosteal changes is mechanically disadvantageous and distinct from typical cortical bone growth, which occurs through a combination of endocortical resorption and periosteal apposition (*27*, *46*). The differential effect of TCM on MAR in the endosteal (endocortical and trabecular) and periosteal compartments may be due to their distinct progenitor cell populations and bone formation pathways (*47*, *48*). This also suggests potential TCM-mediated changes to the bone marrow compartment (e.g., blood vessels), which are known to be altered by tumor-derived factors (*9*) and independently affect bone formation (*49*), and should be tested in future studies. In the trabecular bone, we similarly found that TCM increased bone volume fraction and thickened trabeculae. This is also distinct from the typical pattern of trabecular bone growth and instead mirrors compensatory trabecular thickening mechanisms observed in osteoporosis (*50*). The changes that we observe in bone structure in TCM-injected mice may likewise be due to compensatory growth that facilitates bone's load-bearing function despite altered materials properties (*27*). Both geometric and materials properties of bone influence its response to mechanical forces, which can independently affect tumor growth within bone, possibly through altered bone cell behavior (*51*). Together, these data suggest that TCM induces nonhomeostatic, and potentially pathological, changes to bone structure, which may manifest from altered bone quality. As mice in this study were treated with TCM during a period of rapid skeletal growth to align with the typical age used in bone metastasis studies, future experiments should clarify whether the altered bone growth phenotype that we observed here also translates to settings of bone remodeling in skeletally mature mice. Future work should also explore whether aged and immune-competent mice exhibit similar changes in bone adaptation with TCM treatment, because these factors influence bone cell activity, materials properties, and likelihood of developing bone metastasis (*22*, *52*, *53*).

In contrast to normal new bone, the bone formed during TCM treatment in our study had increased mineral-to-matrix and carbonate-to-mineral ratios (*22*, *36*) as well as a shift in organic matrix composition. In vitro studies have shown that tumor cell–released factors can alter osteoblast metabolism and reduce their production of mineralization-regulating bone matrix proteins collagen I, bone sialoprotein, and osteocalcin (*44*, *54*). Here, we observed decreased levels of the bone matrix protein osteopontin in TCM-treated bones, possibly explaining the increased mineral-to-matrix ratio, as osteopontin can inhibit HA growth and modulate collagen mineralization (*18*, *34*, *37*). While osteopontin was not differentially expressed at the transcriptional level, this could reflect known discrepancies between mRNA and protein levels due to posttranslational factors such as protein stability (*55*). This decrease in osteopontin protein levels in TCM-treated mice is interesting given that osteopontin is typically expressed at lower levels in older bone tissue (*35*) but at high levels in breast cancer (*56*), where it has been found to regulate osteoclast adhesion and activation to support osteolysis (*57*) and contribute to tumor cell adhesion and survival (*58*). However, osteopontin may play contradictory roles in bone and tumors, as its function depends on its phosphorylation and polymerization state (*59*, *60*), warranting further exploration of its contribution to bone metastasis development. Given the shift in organic matrix composition detected via Raman analysis, we expect that bone matrix proteins other than osteopontin, and their respective modifications, may also be of importance to understanding bone mineral alterations during metastatic progression. In addition, the increased carbonate substitution in HA crystals (carbonate-to-mineral ratio) may alter breast cancer cell behavior (*15*, *16*). While tumor cells adhere similarly to mineralized and nonmineralized collagen (*17*), it is possible that altered matrix/mineral properties may still affect DTC survival, growth, and dormancy. More carbonated HA is present during early-stage bone metastasis (*61*), dissolves more easily, and supports osteolytic capability of tumor cells (*15*, *16*) so may even facilitate the transition to osteolysis. This suggests that in the presence of tumor-derived factors, new bone is produced faster with altered mineral and organic matrix properties, which may play a role in facilitating tumor cell attachment to, and growth in, bone (*62*).

Our study highlights the importance of applying multiscale materials analysis techniques in cancer research to complement conventional biological methodologies, which may not be sufficient to detect changes that occur independent of transcriptional variations. Although RNA-seq and histological analysis revealed very few differences between the bones of TCM-treated and control mice, we observed a clear impact of TCM on bone structure and mineral properties via micro-CT and Raman imaging. While future studies are needed to determine whether these TCM-mediated changes (and their underlying mechanisms) actually modulate bone metastasis development, similar modifications to bone matrix have been noted in tumor-bearing mice before any radiologic evidence of bone metastasis (*14*, *61*), suggesting that materials signatures can have diagnostic value if characterized in the context of metastatic progression. Notably, the changes that we observed are location dependent, underscoring the need for correlative, high-resolution tools to facilitate our understanding of the spatiotemporal dynamics of bone microenvironmental alterations and DTC fate. In the future, using synchrotron-based SAXS/wide-angle x-ray scattering (WAXS) would improve spatial resolution for analysis of mineral properties by 10-fold compared to laboratory-source SAXS, potentially enabling specific examination of double-labeled bone matrix as well as in bone interfacing with the growth plate. Advances in image registration for longitudinal micro-CT–based dynamic histomorphometry (*63*), intravital imaging (*6*), and versatile imaging probes (*64*) will be key to accurately pinpointing where relevant changes happen.

Here, using a breast cancer cell line that typically produces osteolytic bone metastases, we provide strong evidence of a bone formation phenotype induced by tumor-derived signals. Given that circulating tumor–derived factors induce bone formation and changes in mineral properties (e.g., carbonate substitution) that may affect DTCs subsequently arriving in the bone, it is possible that they are priming a premetastatic niche to facilitate cancer cell attachment, survival, and ultimately, secondary tumor formation. Further examination of whether these micro- and nanoscale alterations in bone mineral affect bone metastatic progression, whether immunocompetent models exhibit the same changes, and which specific factors drive this process must be fully tested in the future. The application of multiscale and correlative materials characterization techniques not conventionally applied to study bone metastasis may play key roles in unraveling these mechanisms and will define parameters to build better in vitro engineered systems for studying bone metastasis progression (*65*, *66*).

MATERIALS AND METHODS

Animals

This animal study was performed in accordance with the Cornell University animal care guidelines and was approved by Cornell University's Institutional Animal Care and Use Committee. Three-week-old, female athymic nude-*Foxn1*^{nu} mice ($n = 5$ per condition) were purchased from Envigo and housed five animals per cage with ad libitum access to food and water. For 3 weeks, mice received daily intraperitoneal injections of TCM or blank media control. To generate TCM for injections, MDA-MB-231 breast cancer cells (American Type Culture Collection) at 90% confluency were incubated in serum-free Dulbecco's modified Eagle's medium (DMEM) supplemented with 1% penicillin/streptomycin (Invitrogen) for 24 hours. Conditioned medium was collected, normalized to cell number, concentrated 10-fold in an Amicon centrifugal filter unit (molecular weight cutoff, 3 kDa; EMD Millipore), and subsequently diluted fivefold with serum-free DMEM. Each injection (300 μl in volume) delivered conditioned medium that was produced by an equivalent of 280,000 tumor cells [or a multicellular tumor spheroid with a diameter of ~2 to 3 mm (*67*)]. Blank low-serum DMEM was processed similarly (control) for mice receiving control injections. TCM and control treatments were prepared in one batch, frozen in aliquots, and thawed immediately before injection to ensure consistency between injections.

Experimental design

At the end of the treatment period, mice were euthanized by CO_2 administration. From each mouse, one tibia was fixed in 10% neutral-buffered formalin for 48 hours and used for histology; the contralateral tibia was fixed in 70% ethanol for 48 hours and used for micro-CT, BSE, dynamic histomorphometry, Raman, and SAXS analysis; and the femora were used to harvest RNA.

RNA-seq of femora

Because the distal femur is a site also targeted by tumor cells in mouse models, RNA was harvested in bulk from trabecular bone tissue from the distal femora (n = 5 per condition) at the time of tibia collection. Contamination from marrow was prevented by removal via centrifugation, and RNA was extracted using TRIzol (Life Technologies) and the RNeasy Kit (Qiagen) as described previously (*26*). Total RNA was analyzed with a fragment analyzer and then processed using the TruSeq RNA Sample Preparation Kit (Illumina) to create RNA-seq libraries. Libraries were tested using a fragment analyzer to determine the distribution of fragment sizes. The 10 individually bar-coded libraries were normalized, pooled into one lane, and sequenced (75–base pair single-end reads; Illumina NextSeq 500). Sequences were aligned to the mouse genome (GRCm38) using STAR (*68*) and featureCounts (*69*). Differential expression analysis was conducted using the DESeq2 (*70*) and biomaRt R/Bioconductor packages (*71*), with the criteria of adjusted P value of <0.05 and $\log_2$ fold change of >2. Gene set enrichment analysis (GSEA) was conducted using the GSEAPreranked tool (Broad Institute). On the basis of false discovery rates (false discovery rate < 0.25), there were no significant gene set representatives for Gene Ontology Biological Processes.

Micro-CT imaging

To obtain the morphology of mice tibiae, samples (n = 5 in each group) embedded in poly(methyl methacrylate) were scanned with an EasyTom high-resolution x-ray micro-CT system (RX Solutions, France). Scans were performed with voxel sizes of 10.0 μm, at 60-kV source voltage and 166-μA source current, over 360° of sample rotation. The images were visualized using Amira (Thermo Fisher Scientific, USA) and were analyzed by CTAn (Bruker, USA). First, the image datasets were oriented in three dimensions (3D) based on similar anatomic locations of each tibia. The length of the tibia was taken as the distance between the proximal and distal ends. An ROI and a further volume of interest (VOI) were selected along the tibia long axis (from the proximal to distal end) for the trabecular bone and cortical bone. The threshold for each ROI was determined by the histogram of VOI. Images were binarized such that bone appeared as white and all background as black. The proximal tibia exhibits several distinct tissue zones: growth plate, trabecular bone, and cortical bone regions. We followed the definitions from (*72*) and defined the growth plate as including, from proximally to distally, the unmineralized hyaline cartilage, the mineralized cartilage, and some newly formed bone. Beneath the growth plate, the trabecular bone and the cortical bone were manually segmented from each other. For the analysis of the trabecular bone in the tibia, we chose to analyze the volume below the growth plate of 1.1 mm in height because the volume contains most of the trabecular bone. Standard trabecular morphometric variables (e.g., thickness, separation, number, and bone volume/total volume) were quantified in CTAn. For the cortical bone, we chose the volume below the growth plate of 1.9 mm in height with an offset of 1.0 mm distal to the growth plate because this region contains mature cortical bone. Standard cortical bone morphometric variables (e.g., volume and thickness) were quantified in CTAn. The bone cross-sectional area and polar moment of inertia were calculated in BoneJ (*73*).

For further analysis of tibiae, the blocks containing tibiae were cut in half along the coronal plane in similar anatomic locations based on the virtual CT images. One-half of the block with exposed tibia bone was polished with a series of carbide grinding papers and polished with diamond suspension down to 1 μm and lastly polished using 0.25-μm silica suspension for BSE imaging, confocal imaging, and Raman microspectroscopy. The other half of the block was ground to ~100 μm for SAXS measurement.

Backscattered electron microscopy

To visualize the bone mineralization, one-half of the block (n = 4 in each group) was examined with an environmental scanning electron microscope (FEI Quanta 650, Oregon, USA) at 12.5 kV in BSE mode under low-vacuum conditions.

Histology

Following fixation, tibiae were decalcified in 10% EDTA at pH 7.4 for 2 weeks. Histology and IHC were performed on paraffin-embedded sections. Histology staining included hematoxylin and eosin. IHC was used to assess cathepsin K (osteoclasts), procollagen I (osteoblasts), and osteopontin, with antibodies purchased from Abcam, Developmental Studies Hybridoma Bank, and EMD Millipore, respectively. For cathepsin K and osteopontin IHC, the VECTASTAIN Elite ABC Kit (Vector Laboratories) was used. For procollagen I IHC, the Mouse-on-Mouse Kit (Vector Laboratories) was used. Images of stained sections were captured using a Scanscope digital slide scanner (Aperio). Percentage of positive pixels within 200 μm of the growth plate and within 50 μm of a bone surface was quantified using ImageScope software (Aperio).

Confocal laser scanning microscopy

For bone dynamic histomorphometry analysis, mice were injected with calcein (10 mg/kg body weight) and xylenol orange (90 mg/kg body weight) at 9 and 2 days before sacrifice, respectively. To visualize the calcein- and xylenol orange–labeled newly formed bone, the blocks containing exposed tibiae (n = 3 in each group) were investigated using a Leica TCS SP8 confocal laser scanning microscope with 488 and 561 nm lasers and HyD (503 to 530 nm) and HyD (594 to 620 nm) detectors, respectively. Images were processed in Leica Application Suite X software.

Raman microspectroscopy

Raman imaging was acquired using a confocal Raman microscope (CRM200, WITec GmbH, Ulm, Germany) on the block containing exposed tibiae (n = 3 in each group). A 785-nm laser (Toptica Photonics AG, Graefelfing, Germany) with a 20× objective was used to acquire

Raman signals while minimizing autofluorescence. The spectrometer was calibrated using a silicon wafer sample using its 0-cm^{-1} (the Rayleigh scattering) and 520-cm^{-1} (Si-Si vibrational band) peaks. Integration time was 2 s for each spectrum with 2 software accumulations and 10 hardware accumulations. The linearly polarized laser was rotated using a half-wave plate. The resulting Raman data were analyzed using WITec Project software (v.2.10, WITec GmbH, Ulm, Germany). Backgrounds of spectra were removed using the same software. Mineral-to-matrix ratio and carbonate-to-mineral ratio were calculated on the basis of the integrated peak areas of ν_2 PO_4^{3-}/amide III and ν_1 CO_3^{2-}/ν_2 PO_4^{3-}, respectively, because of their insensitivity to the polarization effect of the laser (*29*). The integration ranges of the Raman peaks for ν_2 PO_4^{3-}, ν_1 CO_3^{2-}, amide III, and CH_2-wag were 410 to 460, 1050 to 1100, 1215 to 1350, and 1360 to 1515 cm^{-1}, respectively. Newly formed bone regions in both endocortical bone and trabecular bone were correlatively chosen on the basis of the bone dynamic histomorphometry images and BSE images.

SAXS experiment

The other half of the sample block was ground to ~100 μm for SAXS measurement (n = 3 in each group). The SAXS instrument was equipped with a fine-focus rotating copper-anode generator (CuK_α radiation $\lambda = 0.154$ nm, operating at 40 kV/40 mA), multilayer mirror optics, an evacuated pinhole camera, and a 2D position-sensitive proportional counter with a spatial resolution of 50 μm ("Nanostar," Bruker AXS Karlsruhe, Germany) for recording SAXS patterns. The samples were mounted on a moveable sample holder (movement precision of 2 μm) in the plane perpendicular to the beam (beam diameter, 115 μm). In each location (epiphyseal bone, mineralized cartilage, trabecular bone, and cortical bone), 5 to 10 spots from each sample were chosen.

Considering bone as a two-phase system composed of organic matrix and mineral differing in electron density, three quantities, T, ρ, and $G(x)$, were determined from the SAXS experiments (*74*). The T parameter was obtained from the spherically averaged scattering intensity. It is a measure for the mean mineral particle thickness and is defined as $T = 4\varphi(1-\varphi)/\sigma$ with φ being the mineral volume fraction and σ being the total surface of the mineral particles per total tissue volume. If the mineral particle alignment is perfectly parallel, then the scanning-SAXS pattern shows a narrow streak ($\rho = 1$), whereas completely randomly aligned particles cause a spherically shaped scanning-SAXS pattern ($\rho = 0$). All other configurations of alignment cause elliptically shaped SAXS patterns. Last, the function $G(x)$, which characterizes mineral crystal arrangement (the interparticle distance and the regularity of the distance), was determined as $G(x)Kx^2I(x)$, with x being the product of the scattering vector q and the T parameter, $I(x)$ being the radial intensity. K was chosen so that the integral of $G(x)$ equals one (*75*).

Statistical analyses

For the length, trabecular bone, and cortical bone parameter measurements, an unpaired t test was performed using GraphPad Prism 8.0 (GraphPad Software, La Jolla, CA, USA). For SAXS measurement, because mice tibiae were measured in multiple regions and repeatedly measured within these regions, a mixed model accounting for both fixed and random effects was used. The nested t test (GraphPad Prism 8.0 software) fits a mixed model, where individual animals are assumed random while the mouse strain and the regions are fixed. For the Raman parameters, one-way analysis of variance (ANOVA) with Tukey's multiple comparisons test was used (GraphPad Prism 8.0 software).

SUPPLEMENTARY MATERIALS

Supplementary material for this article is available at http://advances.sciencemag.org/cgi/content/full/7/12/eabf2283/DC1

View/request a protocol for this paper from *Bio-protocol*.

REFERENCES AND NOTES

1. R. E. Coleman, R. D. Rubens, The clinical course of bone metastases from breast cancer. *Br. J. Cancer* **55**, 61–66 (1987).
2. W. Kozlow, T. A. Guise, Breast cancer metastasis to bone: Mechanisms of osteolysis and implications for therapy. *J. Mammary Gland Biol. Neoplasia* **10**, 169–180 (2005).
3. Y. Hüsemann, J. B. Geigl, F. Schubert, P. Musiani, M. Meyer, E. Burghart, G. Forni, R. Eils, T. Fehm, G. Riethmüller, C. A. Klein, Systemic spread is an early step in breast cancer. *Cancer Cell* **13**, 58–68 (2008).
4. R. N. Kaplan, R. D. Riba, S. Zacharoulis, A. H. Bramley, L. Vincent, C. Costa, D. D. MacDonald, D. K. Jin, K. Shido, S. A. Kerns, Z. Zhu, D. Hicklin, Y. Wu, J. L. Port, N. Altorki, E. R. Port, D. Ruggero, S. V. Shmelkov, K. K. Jensen, S. Rafii, D. Lyden, VEGFR1-positive haematopoietic bone marrow progenitors initiate the pre-metastatic niche. *Nature* **438**, 820–827 (2005).
5. T. R. Cox, R. M. H. Rumney, E. M. Schoof, L. Perryman, A. M. Høye, A. Agrawal, D. Bird, N. A. Latif, H. Forrest, H. R. Evans, I. D. Huggins, G. Lang, R. Linding, A. Gartland, J. T. Erler, The hypoxic cancer secretome induces pre-metastatic bone lesions through lysyl oxidase. *Nature* **522**, 106–110 (2015).
6. T. T. Price, M. L. Burness, A. Sivan, M. J. Warner, R. Cheng, C. H. Lee, L. Olivere, K. Comatas, J. Magnani, H. K. Lyerly, Q. Cheng, C. M. McCall, D. A. Sipkins, Dormant breast cancer micrometastases reside in specific bone marrow niches that regulate their transit to and from bone. *Sci. Transl. Med.* **8**, 340ra73 (2016).
7. P. Carlson, A. Dasgupta, C. A. Grzelak, J. Kim, A. Barrett, I. M. Coleman, R. E. Shor, E. T. Goddard, J. Dai, E. M. Schweitzer, A. R. Lim, S. B. Crist, D. A. Cheresh, P. S. Nelson, K. C. Hansen, C. M. Ghajar, Targeting the perivascular niche sensitizes disseminated tumour cells to chemotherapy. *Nat. Cell Biol.* **21**, 238–250 (2019).
8. L. E. Barney, C. L. Hall, A. D. Schwartz, A. N. Parks, C. Sparages, S. Galarza, M. O. Platt, A. M. Mercurio, S. R. Peyton, Tumor cell–organized fibronectin maintenance of a dormant breast cancer population. *Sci. Adv.* **6**, eaaz4157 (2020).
9. C. M. Ghajar, H. Peinado, H. Mori, I. R. Matei, K. J. Evason, H. Brazier, D. Almeida, A. Koller, K. A. Hajjar, D. Y. R. Stainier, E. I. Chen, D. Lyden, M. J. Bissell, The perivascular niche regulates breast tumour dormancy. *Nat. Cell Biol.* **15**, 807–817 (2013).
10. H. Wang, L. Tian, J. Liu, A. Goldstein, I. Bado, W. Zhang, B. R. Arenkiel, Z. Li, M. Yang, S. Du, H. Zhao, D. R. Rowley, S. T. C. Wong, Z. Gugala, X. H.-F. Zhang, The osteogenic niche is a calcium reservoir of bone micrometastases and confers unexpected therapeutic vulnerability. *Cancer Cell* **34**, 823–839.e7 (2018).
11. H. Wang, C. Yu, X. Gao, T. Welte, A. M. Muscarella, L. Tian, H. Zhao, Z. Zhao, S. Du, J. Tao, B. Lee, T. F. Westbrook, S. T. C. Wong, X. Jin, J. M. Rosen, C. K. Osborne, X. H.-F. Zhang, The osteogenic niche promotes early-stage bone colonization of disseminated breast cancer cells. *Cancer Cell* **27**, 193–210 (2015).
12. N. Wang, F. E. Docherty, H. K. Brown, K. J. Reeves, A. C. M. Fowles, P. D. Ottewell, T. N. Dear, I. Holen, P. I. Croucher, C. L. Eaton, Prostate cancer cells preferentially home to osteoblast-rich areas in the early stages of bone metastasis: Evidence from in vivo models. *J. Bone Miner. Res.* **29**, 2688–2696 (2014).
13. A. Gartland, J. T. Erler, T. R. Cox, The role of lysyl oxidase, the extracellular matrix and the pre-metastatic niche in bone metastasis. *J. Bone Oncol.* **5**, 100–103 (2016).
14. F. He, A. E. Chiou, H. C. Loh, M. Lynch, B. R. Seo, Y. H. Song, M. J. Lee, R. Hoerth, E. L. Bortel, B. M. Willie, G. N. Duda, L. A. Estroff, A. Masic, W. Wagermaier, P. Fratzl, C. Fischbach, Multiscale characterization of the mineral phase at skeletal sites of breast cancer metastasis. *Proc. Natl. Acad. Sci. U.S.A.* **114**, 10542–10547 (2017).
15. S. P. Pathi, D. D. W. Lin, J. R. Dorvee, L. A. Estroff, C. Fischbach, Hydroxyapatite nanoparticle-containing scaffolds for the study of breast cancer bone metastasis. *Biomaterials* **32**, 5112–5122 (2011).
16. S. Choi, S. Coonrod, L. Estroff, C. Fischbach, Chemical and physical properties of carbonated hydroxyapatite affect breast cancer cell behavior. *Acta Biomater.* **24**, 333–342 (2015).
17. S. Choi, J. Friedrichs, Y. H. Song, C. Werner, L. A. Estroff, C. Fischbach, Intrafibrillar, bone-mimetic collagen mineralization regulates breast cancer cell adhesion and migration. *Biomaterials* **198**, 95–106 (2019).
18. P. Fratzl, R. Weinkamer, Nature's hierarchical materials. *Prog. Mater. Sci.* **52**, 1263–1334 (2007).
19. T. A. Guise, The vicious cycle of bone metastases. *J. Musculoskelet. Neuronal Interact.* **2**, 570–572 (2002).

20. M. V. Burke, A. Atkins, M. Akens, T. L. Willett, C. M. Whyne, Osteolytic and mixed cancer metastasis modulates collagen and mineral parameters within rat vertebral bone matrix. *J. Orthop. Res.* **34**, 2126–2136 (2016).
21. X. Bi, J. A. Sterling, A. R. Merkel, D. S. Perrien, J. S. Nyman, A. Mahadevan-Jansen, Prostate cancer metastases alter bone mineral and matrix composition independent of effects on bone architecture in mice –– a quantitative study using microCT and Raman spectroscopy. *Bone* **56**, 454–460 (2013).
22. E. Donnelly, A. L. Boskey, S. P. Baker, M. C. H. van der Meulen, Effects of tissue age on bone tissue material composition and nanomechanical properties in the rat cortex. *J. Biomed. Mater. Res. A.* **92**, 1048–1056 (2010).
23. G. Allocca, R. Hughes, N. Wang, H. K. Brown, P. D. Ottewell, N. J. Brown, I. Holen, The bone metastasis niche in breast cancer: Potential overlap with the haematopoietic stem cell niche *in vivo*. *J. Bone Oncol.* **17**, 100244 (2019).
24. Y. Kang, P. M. Siegel, W. Shu, M. Drobnjak, S. M. Kakonen, C. Cordón-Cardo, T. A. Guise, J. Massagué, A multigenic program mediating breast cancer metastasis to bone. *Cancer Cell* **3**, 537–549 (2003).
25. G. Allocca, A. P. Kusumbe, S. K. Ramasamy, N. Wang, Confocal/two-photon microscopy in studying colonisation of cancer cells in bone using xenograft mouse models. *Bonekey Rep.* **5**, 851 (2016).
26. N. H. Kelly, J. C. Schimenti, F. Patrick Ross, M. C. H. van der Meulen, A method for isolating high quality RNA from mouse cortical and cancellous bone. *Bone* **68**, 1–5 (2014).
27. M. C. H. van der Meulen, K. J. Jepsen, B. Mikić, Understanding bone strength: Size isn't everything. *Bone* **29**, 101–104 (2001).
28. P. A. Phadke, R. R. Mercer, J. F. Harms, Y. Jia, A. R. Frost, J. L. Jewell, K. M. Bussard, S. Nelson, C. Moore, J. C. Kappes, C. V. Gay, A. M. Mastro, D. R. Welch, Kinetics of metastatic breast cancer cell trafficking in bone. *Clin. Cancer Res.* **12**, 1431–1440 (2006).
29. M. Kazanci, H. D. Wagner, N. I. Manjubala, H. S. Gupta, E. Paschalis, P. Roschger, P. Fratzl, Raman imaging of two orthogonal planes within cortical bone. *Bone* **41**, 456–461 (2007).
30. S. Gamsjaeger, A. Masic, P. Roschger, M. Kazanci, J. W. C. Dunlop, K. Klaushofer, E. P. Paschalis, P. Fratzl, Cortical bone composition and orientation as a function of animal and tissue age in mice by Raman spectroscopy. *Bone* **47**, 392–399 (2010).
31. E. R. C. Draper, M. D. Morris, N. P. Camacho, P. Matousek, M. Towrie, A. W. Parker, A. E. Goodship, Novel assessment of bone using time-resolved transcutaneous raman spectroscopy. *J. Bone Miner. Res.* **20**, 1968–1972 (2005).
32. Y. Ishimaru, Y. Oshima, Y. Imai, T. Iimura, S. Takanezawa, K. Hino, H. Miura, Raman spectroscopic analysis to detect reduced bone quality after sciatic neurectomy in mice. *Molecules* **23**, 3081 (2018).
33. M. D'Acunto, R. Gaeta, R. Capanna, A. Franchi, Contribution of raman spectroscopy to diagnosis and grading of chondrogenic tumors. *Sci. Rep.* **10**, 2155 (2020).
34. A. L. Boskey, L. Spevak, E. Paschalis, S. B. Doty, M. D. McKee, Osteopontin deficiency increases mineral content and mineral crystallinity in mouse bone. *Calcif. Tissue Int.* **71**, 145–154 (2002).
35. G. E. Sroga, L. Karim, W. Colón, D. Vashishth, Biochemical characterization of major bone-matrix proteins using nanoscale-size bone samples and proteomics methodology. *Mol. Cell. Proteomics* **10**, M110.006718 (2011).
36. E. P. Paschalis, E. DiCarlo, F. Betts, P. Sherman, R. Mendelsohn, A. L. Boskey, FTIR microspectroscopic analysis of human osteonal bone. *Calcif. Tissue Int.* **59**, 480–487 (1996).
37. D. E. Rodriguez, T. Thula-Mata, E. J. Toro, Y.-W. Yeh, C. Holt, L. S. Holliday, L. B. Gower, Multifunctional role of osteopontin in directing intrafibrillar mineralization of collagen and activation of osteoclasts. *Acta Biomater.* **10**, 494–507 (2014).
38. C. H. Van Poznak, The use of bisphosphonates in patients with breast cancer. *Cancer Control* **9**, 480–489 (2002).
39. Early Breast Cancer Trialists' Collaborative Group (EBCTCG), Adjuvant bisphosphonate treatment in early breast cancer: Meta-analyses of individual patient data from randomised trials. *Lancet* **386**, 1353–1361 (2015).
40. H. Zheng, Y. Kang, Cradle of evil: Osteogenic niche for early bone metastasis. *Cancer Cell* **27**, 153–155 (2015).
41. Y. Liu, X. Cao, Characteristics and significance of the pre-metastatic niche. *Cancer Cell* **30**, 668–681 (2016).
42. A. D. Kolb, A. B. Shupp, D. Mukhopadhyay, F. C. Marini, K. M. Bussard, Osteoblasts are "educated" by crosstalk with metastatic breast cancer cells in the bone tumor microenvironment. *Breast Cancer Res.* **21**, 31 (2019).
43. H. Peinado, H. Zhang, I. R. Matei, B. Costa-Silva, A. Hoshino, G. Rodrigues, B. Psaila, R. N. Kaplan, J. F. Bromberg, Y. Kang, M. J. Bissell, T. R. Cox, A. J. Giaccia, J. T. Erler, S. Hiratsuka, C. M. Ghajar, D. Lyden, Pre-metastatic niches: Organ-specific homes for metastases. *Nat. Rev. Cancer* **17**, 302–317 (2017).
44. A. Loftus, A. Cappariello, C. George, A. Ucci, K. Shefferd, A. Green, R. Paone, M. Ponzetti, S. Delle Monache, M. Muraca, A. Teti, N. Rucci, Extracellular vesicles from osteotropic breast cancer cells affect bone resident cells. *J. Bone Miner. Res.* **35**, 396–412 (2020).
45. F. He, N. L. Springer, M. A. Whitman, S. P. Pathi, Y. Lee, S. Mohanan, S. Marcott, A. E. Chiou, B. S. Blank, N. Iyengar, P. G. Morris, M. Jochelson, C. A. Hudis, P. Shah, J. A. M. R. Kunitake, L. A. Estroff, J. Lammerding, C. Fischbach, Hydroxyapatite mineral enhances malignant potential in a tissue-engineered model of ductal carcinoma *in situ* (DCIS). *Biomaterials* **224**, 119489 (2019).
46. C. B. Ruff, W. C. Hayes, Subperiosteal expansion and cortical remodeling of the human femur and tibia with aging. *Science* **217**, 945–948 (1982).
47. A. Roschger, W. Wagermaier, S. Gamsjaeger, N. Hassler, I. Schmidt, S. Blouin, A. Berzlanovich, G. M. Gruber, R. Weinkamer, P. Roschger, E. P. Paschalis, K. Klaushofer, P. Fratzl, Newly formed and remodeled human bone exhibits differences in the mineralization process. *Acta Biomater.* **104**, 221–230 (2020).
48. S. Debnath, A. R. Yallowitz, J. M. Cormick, S. Lalani, T. Zhang, R. Xu, N. Li, Y. Liu, Y. S. Yang, M. Eiseman, J.-H. Shim, M. Hameed, J. H. Healey, M. P. Bostrom, D. A. Landau, M. B. Greenblatt, Discovery of a periosteal stem cell mediating intramembranous bone formation. *Nature* **562**, 133–139 (2018).
49. A. P. Kusumbe, S. K. Ramasamy, R. H. Adams, Coupling of angiogenesis and osteogenesis by a specific vessel subtype in bone. *Nature* **507**, 323–328 (2014).
50. A. M. Parfitt, C. H. E. Mathews, A. R. Villanueva, M. Kleerekoper, B. Frame, D. S. Rao, Relationships between surface, volume, and thickness of iliac trabecular bone in aging and in osteoporosis. Implications for the microanatomic and cellular mechanisms of bone loss. *J. Clin. Invest.* **72**, 1396–1409 (1983).
51. M. E. Lynch, D. Brooks, S. Mohanan, M. J. Lee, P. Polamraju, K. Dent, L. J. Bonassar, M. C. H. van der Meulen, C. Fischbach, In vivo tibial compression decreases osteolysis and tumor formation in a human metastatic breast cancer model. *J. Bone Miner. Res.* **28**, 2357–2367 (2013).
52. N. Wang, K. J. Reeves, H. K. Brown, A. C. M. Fowles, F. E. Docherty, P. D. Ottewell, P. I. Croucher, I. Holen, C. L. Eaton, The frequency of osteolytic bone metastasis is determined by conditions of the soil, not the number of seeds; evidence from in vivo models of breast and prostate cancer. *J. Exp. Clin. Cancer Res.* **34**, 124 (2015).
53. X. Luo, Y. Fu, A. J. Loza, B. Murali, K. M. Leahy, M. K. Ruhland, M. Gang, X. Su, A. Zamani, Y. Shi, K. J. Lavine, D. M. Ornitz, K. N. Weilbaecher, F. Long, D. V. Novack, R. Faccio, G. D. Longmore, S. A. Stewart, Stromal-initiated changes in the bone promote metastatic niche development. *Cell Rep.* **14**, 82–92 (2016).
54. R. R. Mercer, C. Miyasaka, A. M. Mastro, Metastatic breast cancer cells suppress osteoblast adhesion and differentiation. *Clin. Exp. Metastasis* **21**, 427–435 (2004).
55. S. P. Gygi, Y. Rochon, B. R. Franza, R. Aebersold, Correlation between protein and mRNA abundance in yeast. *Mol. Cell. Biol.* **19**, 1720–1730 (1999).
56. A. Bellahcène, V. Castronovo, K. U. E. Ogbureke, L. W. Fisher, N. S. Fedarko, Small integrin-binding ligand N-linked glycoproteins (SIBLINGs): Multifunctional proteins in cancer. *Nat. Rev. Cancer* **8**, 212–226 (2008).
57. T. Ibrahim, I. Leong, O. Sanchez-Sweatman, R. Khokha, J. Sodek, H. C. Tenenbaum, B. Ganss, S. Cheifetz, Expression of bone sialoprotein and osteopontin in breast cancer bone metastases. *Clin. Exp. Metastasis* **18**, 253–260 (2000).
58. T. E. Kruger, A. H. Miller, A. K. Godwin, J. Wang, Bone sialoprotein and osteopontin in bone metastasis of osteotropic cancers. *Crit. Rev. Oncol. Hematol.* **89**, 330–341 (2014).
59. A. Gericke, C. Qin, L. Spevak, Y. Fujimoto, W. T. Butler, E. S. Sørensen, A. L. Boskey, Importance of phosphorylation for osteopontin regulation of biomineralization. *Calcif. Tissue Int.* **77**, 45–54 (2005).
60. B. Hoac, V. Nelea, W. Jiang, M. T. Kaartinen, M. D. McKee, Mineralization-inhibiting effects of transglutaminase-crosslinked polymeric osteopontin. *Bone* **101**, 37–48 (2017).
61. C. Zhang, P. T. Winnard Jr., S. Dasari, S. L. Kominsky, M. Doucet, S. Jayaraman, V. Raman, I. Barman, Label-free Raman spectroscopy provides early determination and precise localization of breast cancer-colonized bone alterations. *Chem. Sci.* **9**, 743–753 (2018).
62. K. Pantel, R. H. Brakenhoff, B. Brandt, Detection, clinical relevance and specific biological properties of disseminating tumour cells. *Nat. Rev. Cancer* **8**, 329–340 (2008).
63. C. M. J. de Bakker, A. R. Altman, W.-J. Tseng, M. B. Tribble, C. Li, A. Chandra, L. Qin, X. S. Liu, μCT-based, in vivo dynamic bone histomorphometry allows 3D evaluation of the early responses of bone resorption and formation to PTH and alendronate combination therapy. *Bone* **73**, 198–207 (2015).
64. A. E. Chiou, J. A. Hinckley, R. Khaitan, N. Varsano, J. Wang, H. F. Malarkey, C. J. Hernandez, R. M. Williams, L. A. Estroff, S. Weiner, L. Addadi, U. B. Wiesner, C. Fischbach, Fluorescent silica nanoparticles to label metastatic tumor cells in mineralized bone microenvironments. *Small* **2020**, 2001432 (2020).
65. E. C. González Díaz, S. Sinha, R. S. Avedian, F. Yang, Tissue-engineered 3D models for elucidating primary and metastatic bone cancer progression. *Acta Biomater.* **99**, 18–32 (2019).
66. W. Zhu, M. Wang, Y. Fu, N. J. Castro, S. W. Fu, L. G. Zhang, Engineering a biomimetic three-dimensional nanostructured bone model for breast cancer bone metastasis study. *Acta Biomater.* **14**, 164–174 (2015).
67. L. Ling, J. A. Mulligan, Y. Ouyang, A. A. Shimpi, R. M. Williams, G. F. Beeghly, B. D. Hopkins, J. A. Spector, S. G. Adie, C. Fischbach, Obesity-associated adipose stromal cells promote breast cancer invasion through direct cell contact and ECM remodeling. *Adv. Funct. Mater.* **30**, 1910650 (2020).

68. A. Dobin, C. A. Davis, F. Schlesinger, J. Drenkow, C. Zaleski, S. Jha, P. Batut, M. Chaisson, T. R. Gingeras, STAR: Ultrafast universal RNA-seq aligner. *Bioinformatics* **29**, 15–21 (2013).
69. Y. Liao, G. K. Smyth, W. Shi, FeatureCounts: An efficient general purpose program for assigning sequence reads to genomic features. *Bioinformatics* **30**, 923–930 (2014).
70. M. I. Love, W. Huber, S. Anders, Moderated estimation of fold change and dispersion for RNA-seq data with DESeq2. *Genome Biol.* **15**, 550 (2014).
71. S. Durinck, P. T. Spellman, E. Birney, W. Huber, Mapping identifiers for the integration of genomic datasets with the R/Bioconductor package biomaRt. *Nat. Protoc.* **4**, 1184–1191 (2009).
72. H. Haimov, E. Shimoni, V. Brumfeld, M. Shemesh, N. Varsano, L. Addadi, S. Weiner, Mineralization pathways in the active murine epiphyseal growth plate. *Bone* **130**, 115086 (2020).
73. M. Doube, M. M. Kłosowski, I. Arganda-Carreras, F. P. Cordelières, R. P. Dougherty, J. S. Jackson, B. Schmid, J. R. Hutchinson, S. J. Shefelbine, BoneJ: Free and extensible bone image analysis in ImageJ. *Bone* **47**, 1076–1079 (2010).
74. P. Fratzl, N. Fratzl-Zelman, K. Klaushofer, G. Vogl, K. Koller, Nucleation and growth of mineral crystals in bone studied by small-angle X-ray scattering. *Calcif. Tissue Int.* **48**, 407–413 (1991).
75. P. Fratzl, S. Schreiber, K. Klaushofer, Bone mineralization as studied by small-angle x-ray scattering. *Connect. Tissue Res.* **34**, 247–254 (1996).

Acknowledgments: We thank D. Werner for assistance with SAXS and B. Schonert for sample preparation (both from Max Planck Institute of Colloids and Interfaces, Potsdam), as well as B. Cosgrove for help with RNA-seq data interpretation, L. Estroff for helpful discussions about biomineralization, and M. van der Meulen for structural and bone quality data interpretation with respect to mechanical adaptation. We would like to thank the Cornell Center for Animal Resources and Education (CARE) staff for animal care and the Cornell Histology Core for paraffin embedding and sectioning. **Funding:** Research reported in this publication was supported by the Human Frontier Science Program (HFSP RGP0016/2017 to C.F. and P.F.) and the National Cancer Institute of the National Institutes of Health (NIH) under the following award numbers: F31CA228448 (to A.E.C.) and U54CA210184 (Center on the Physics of Cancer Metabolism, to C.F.). The content is solely the responsibility of the authors and does not necessarily represent the official views of the NIH. I.M.-J. acknowledges funding from the Humboldt Foundation. **Author contributions:** A.E.C., C.L., W.W., M.N.D., C.F., and P.F. designed experiments. A.E.C., C.L., and T.T. performed research. A.E.C., C.L., T.T., W.W., I.M.-J., M.N.D., C.F., and P.F. analyzed data. M.N.D., C.F., and P.F. supervised the work. A.E.C., C.L., I.M.-J., M.N.D., C.F., and P.F. wrote the paper. **Competing interests:** The authors declare that they have no competing interests. **Data and materials availability:** All data needed to evaluate the conclusions in the paper are present in the paper and/or the Supplementary Materials. Additional data related to this paper may be requested from the authors.

Submitted 12 October 2020
Accepted 27 January 2021
Published 17 March 2021
10.1126/sciadv.abf2283

Citation: A. E. Chiou, C. Liu, I. Moreno-Jiménez, T. Tang, W. Wagermaier, M. N. Dean, C. Fischbach, P. Fratzl, Breast cancer–secreted factors perturb murine bone growth in regions prone to metastasis. *Sci. Adv.* **7**, eabf2283 (2021).

Science Advances

Breast cancer–secreted factors perturb murine bone growth in regions prone to metastasis

Aaron E. Chiou, Chuang Liu, Inés Moreno-Jiménez, Tengteng Tang, Wolfgang Wagermaier, Mason N. Dean, Claudia Fischbach and Peter Fratzl

Sci Adv **7** (12), eabf2283.
DOI: 10.1126/sciadv.abf2283

Science Advances (ISSN 2375-2548) is published by the American Association for the Advancement of Science, 1200 New York Avenue NW, Washington, DC 20005. The title *Science Advances* is a registered trademark of AAAS.